Journal of Applied Physics ARTICLE scitation.org/journal/jap

Tight-binding band structure of β- and α-phase Ga_2O_3 and Al_2O_3

Cite as: J. Appl. Phys. **131**, 175702 (2022); doi: 10.1063/5.0074598
Submitted: 9 October 2021 · Accepted: 22 March 2022 ·
Published Online: 3 May 2022

Y. Zhang,[1,a)] M. Liu,[2] D. Jena,[1,2] and G. Khalsa[2,b)]

AFFILIATIONS

[1]Electrical and Computer Engineering, Cornell University, Ithaca, New York 14850, USA
[2]Materials Science and Engineering, Cornell University, Ithaca, New York 14850, USA

Note: This paper is part of the Special Topic on Wide Bandgap Semiconductor Materials and Devices.
[a)]**Author to whom correspondence should be addressed:** yz2439@cornell.edu
[b)]**Electronic mail:** guru.khalsa@cornell.edu

ABSTRACT

Rapid design and development of the emergent ultrawide-bandgap semiconductors Ga_2O_3 and Al_2O_3 require a compact model of their electronic structures, accurate over the broad energy range accessed in future high-field, high-frequency, and high-temperature electronics and visible and ultraviolet photonics. A minimal tight-binding model is developed to reproduce the first-principles electronic structures of the β- and α-phases of Ga_2O_3 and Al_2O_3 throughout their reciprocal spaces. Application of this model to α-Ga_2O_3/α-Al_2O_3 superlattices reveals that intersubband transitions can be engineered to the 1.55 μm telecommunications wavelength, opening new directions in oxide photonics. Furthermore, by accurately reproducing the bandgap, orbital character, effective mass, and high-energy features of the conduction band, this compact model will assist in the investigation and design of the electrical and optical properties of bulk materials, devices, and quantum confined heterostructures.

I. INTRODUCTION

The recent integration of Ga_2O_3 with Al_2O_3 has the potential to revolutionize high-power electronics. The availability of large, inexpensive, single-crystal substrates;[1,2] recent advances in thin film growth;[3–5] and the ability to dope these wide-bandgap semiconductors have enabled transistors and Schottky diodes based on β-Ga_2O_3 with breakdown fields as large as 5.45 MV/cm (Ref. 6) and 5.7 MV/cm (Ref. 7) and approaching the projected theoretical estimate of 8 MV/cm (Ref. 8). Comparing these breakdown fields with the existing technological semiconductors Si (0.3 MV/cm), SiC (3.1 MV/cm), and GaN (3.3 MV/cm),[9] β-Ga_2O_3 promises new high-frequency, high-voltage, and high-temperature electronics applications. α-Ga_2O_3 and α-Al_2O_3 further expand the bandgap to 5.2 and 8.8 eV, signifying the potential for oxide semiconductors to expand the future electronics and photonics materials tool-set.

The successful design of these future electronic and photonics devices requires accurate modeling and understanding of the electronic structure and bonding of Ga_2O_3 and Al_2O_3. The tight-binding method provides a flexible, chemically motivated description of the electronic structure of materials.[10] When compared with modern computational approaches to materials physics, such as density functional theory (DFT), tight-binding models are compact, intuitive, and require less computational resources. As a result, tight-binding models are ubiquitous in device engineering and development and have successfully described electronic transport[11–15] and optical properties[14,16–18] of bulk materials, heterostructures, and devices. To aid in the development of new high-power electronics, we derive semi-empirical tight-binding models in this work for three technologically relevant oxide semiconductors: β-Ga_2O_3, α-Ga_2O_3, and α-Al_2O_3.

While we are unaware of a tight-binding model describing these three oxide semiconductors, a recent study reports a tight-binding model of β-Ga_2O_3 using atomic orbitals as a basis, with parameters drawn from DFT calculations.[19] The authors employ the model to study the surface energy of β-Ga_2O_3 and formation energy of Ga and O vacancy defects. We derive an alternative tight-binding model with the goal of accurate parameterization of

the conduction band and fundamental optical gaps of β-Ga_2O_3, α-Ga_2O_3, and α-Al_2O_3 so that electrical and optical properties can be faithfully simulated.

We derive tight-binding models using a Wannier function basis. Wannier functions are a convenient basis for tight-binding models because they are derived from the underlying band structure of the material, are formally orthogonal, can be localized to atomic sites, and preserve the site symmetry and coordination. This approach of DFT-derived tight-binding has been used successfully to describe the electronic structure of broad classes of technologically important materials, including silicon,[20] III–V semiconductors,[21] and 2D materials.[22] An alternative construction using atomic orbitals is also common with several numerical packages available.[23,24]

This article is organized as follows. We first discuss the crystal and electronic structure of β-Ga_2O_3, α-Ga_2O_3, and α-Al_2O_3. We then derive the tight-binding model and compare the tight-binding band structure with the DFT band structure. As an application of the tight-binding model, we study α-Ga_2O_3/α-Al_2O_3 superlattices and discuss the confined electronic structure. Finally, we discuss the additional application of this model.

II. CRYSTAL AND ELECTRONIC STRUCTURE

A. Crystal structure and chemical bonding

The crystal symmetry and bonding environment constrain the tight-binding description of the electronic structure. When compared to a conventional semiconductor such as Si, Ga_2O_3 and Al_2O_3 have relatively low symmetry and complicated bonding networks. β-Ga_2O_3 has a monoclinic structure (space group C2/m, No. 12). The monoclinic structure contains two pairs of symmetry inequivalent Ga sites, each coordinated by O, forming two distorted GaO_4 tetrahedra and two distorted GaO_6 octahedra per unit cell [Fig. 1(a)]. α-Al_2O_3 and α-Ga_2O_3 crystallize in the sapphire structure (rhombohedral, space group R-3c, No. 167). In the α phase, the Al(Ga) atoms occupy four equivalent sites, each coordinated by six O, forming distorted $AlO_6(GaO_6)$ octahedra [Fig. 1(b)]. The structural information obtained from DFT structural optimization and experimental data are given in Table I, where DFT is shown to describe the experimental structure surprisingly well. The valence configurations of O, Al, and Ga are $2s^22p^4$, $3s^23p^1$, and $4s^24p^1$, respectively. The Al(Ga) is expected to donate its valence electrons in order to fill the O valence shell, leading to an O-2p derived valence band with Al-3s(Ga-4s) and Al-3p(Ga-4p) derived conduction bands.

B. First-principles calculations

Structural optimization and electronic band structure are calculated by DFT using Quantum Espresso.[25] We choose projector-augmented wave pseudopotentials and generalized-gradient approximation of exchange correlation using the Perdew–Burke–Ernzerhof functional generalized for solids.[26,27] Structural convergence is found for a $3 \times 3 \times 3$ k-point mesh and a 60 Ry plane-wave cutoff. We find good agreement between the DFT-relaxed structure and the experimental structure (see Table I).

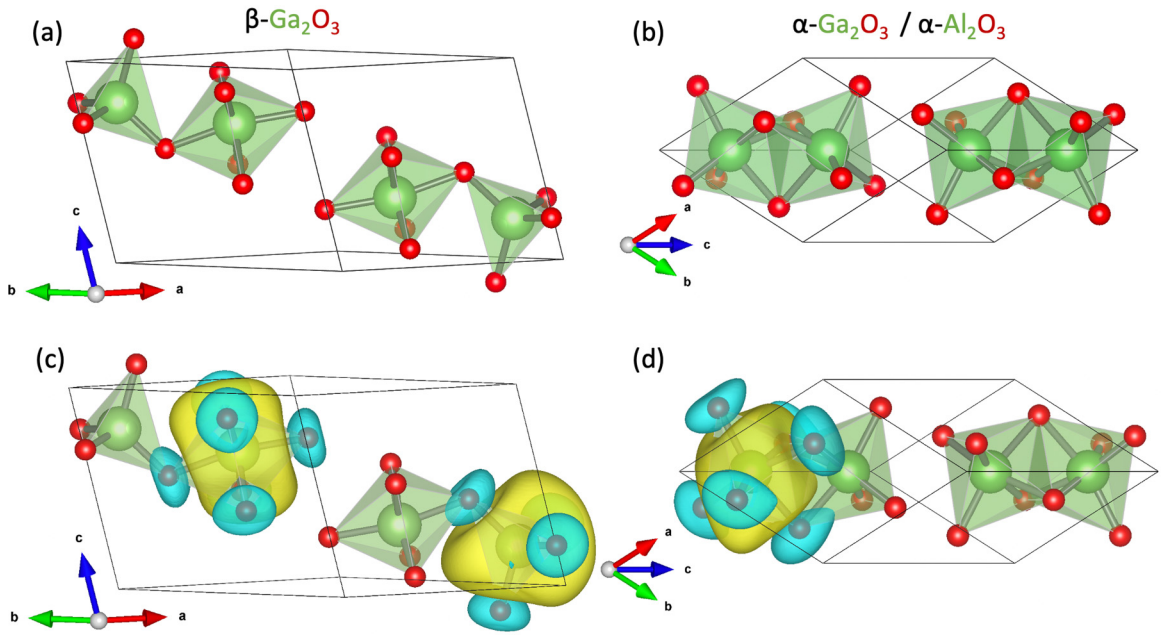

FIG. 1. Crystal structure of monoclinic β-Ga_2O_3 and rhombohedral α-Ga_2O_3 and α-Al_2O_3. Coordination octahedra and tetrahedra highlight the different Ga(Al)-O bonding environments in the β (a) and α (b) phases. This bonding difference is evident in the symmetry of Ga(Al)-site Wannier functions [(c) and (d)] for the conduction band where clear hybridization of the Ga(Al)-s and O-p is seen. In (c) and (d), the positive lobes of the Wannier functions are shown in yellow and the negative lobes in blue.

TABLE I. β-Ga_2O_3, α-Ga_2O_3, and α-Al_2O_3 structural data. In the β-phase (left column), Ga and O occupy the *i* Wyckoff site with fractional coordinates (x, 0, z) and ($-x$, 0, $-z$). In the α phase (right column), Ga(Al) occupies the *c* Wyckoff site with fractional coordinates (z, z, z), $(-z+\frac{1}{2}, -z+\frac{1}{2}, -z+\frac{1}{2})$, $(-z, -z, -z)$, and $(z+\frac{1}{2}, z+\frac{1}{2}, z+\frac{1}{2})$ and *O* occupies the *e* Wyckoff site with fractional coordinates $(x+\frac{1}{4}, -x+\frac{1}{4}, \frac{1}{4})$, $(\frac{1}{4}, x+\frac{1}{4}, -x+\frac{1}{4})$, $(-x+\frac{1}{4}, \frac{1}{4}, x+\frac{1}{4})$, $(-x+\frac{3}{4}, x+\frac{3}{4}, \frac{3}{4})$, $(\frac{3}{4}, -x+\frac{3}{4}, x+\frac{3}{4})$, and $(x+\frac{3}{4}, \frac{3}{4}, -x+\frac{3}{4})$.

β-Ga_2O_3	a (Å)	b (Å)	c (Å)	β (°)
DFT	12.237	3.062	5.813	103.81
Experiment[28]	12.214	3.037	5.798	103.83

	Ga(I) (4i)		Ga(II) (4i)	
β-Ga_2O_3	x	z	x	z
DFT	0.0904	0.7949	0.6585	0.3137
Experiment[28]	0.0895	0.7938	0.6585	0.3100

	O(I) (4i)		O(II) (4i)		O(III) (4i)	
β-Ga_2O_3	x	z	x	z	x	z
DFT	0.1647	0.1094	0.1733	0.5632	0.4959	0.2563
Experiment[28]	0.1519	0.1001	0.1722	0.5640	0.4920	0.2645

α-Ga_2O_3	a (Å)	b (Å)	Ga(I) 4c	O(I) 6e
DFT	5.3221	55.82	$z = 0.1446$	$x = 0.3049$
Experiment[29]	5.3221	55.82	$z = 0.1446$	$x = 0.3049$

α-Al_2O_3	a (Å)	b (Å)	Al(I) 4c	O(I) 6e
DFT	5.1779	55.28	$z = 0.1479$	$x = 0.3056$
Experiment[30]	5.126	55.25	$z = 0.1477$	$x = 0.3064$

C. Electronic band structure

The DFT band structure and DOS are shown in Figs. 2(c), 2(f), and 2(i) and found to be in agreement with the previous work.[31] Orbital-projected DOS shows that the valence band is primarily O-2p, and the conduction band is primarily Ga-4s(Al-3s) and Ga-4p (Al-3p). The bottom of the conduction band is dominated by Ga-4s (Al-3s) states, transitioning to mainly Ga-4p(Al-3p) in character at 6 eV above the conduction band minimum. All three materials share several broad features of their band structure: broad O-2p valence bands with flat valence band edges, conduction band edge features near the Γ point, and indirect bandgaps. In all three materials, the valence band edge is populated by flat O-2p bands. DFT predicts the valence band maximum between M_2 and D in β-Ga_2O_3 and between Γ and S_0 in both α-Ga_2O_3 and α-Al_2O_3. The conduction band minimum at the Γ-point has nearly isotropic dispersion, suggesting that it is insensitive to symmetry and chemistry. We find an effective mass of $0.26m_e$ in β-Ga_2O_3, $0.28m_e$ in α-Ga_2O_3, and $0.42m_e$ in α-Al_2O_3, where m_e is the electron effective mass. We find that the conduction band effective mass of β-Ga_2O_3 is in good agreement with recent transport[32] and angle-resolved photoemission spectroscopy[33,34] (ARPES) experiments. Away from the band minimum, the conduction band transitions from parabolic to linear dispersion, a bandstructure feature used to explain high-field transport[35,36] and optical absorption[37] experiments. The second conduction band at the Γ point is above the conduction band minimum by 3.3 eV in β-Ga_2O_3, 3.5 eV in α-Ga_2O_3, and 3.1 eV in α-Al_2O_3, respectively. The value of β-Ga_2O_3 agrees with the experimental observation of 3.55 eV.[37] DFT predicts an indirect bandgap with the difference between the direct and indirect bandgap less than 20 meV. This is confirmed by the ARPES measurement.[33,34] As expected, the bandgap predicted by DFT underestimates the experimental bandgaps. In order to match the experimental bandgap, we have conducted a "scissor cut" by shifting the conduction band states up in energy so that the bandgaps match the experimental values of 4.9,[34] 5.2,[38] and 8.8 eV[39] in β-Ga_2O_3, α-Ga_2O_3, and α-Al_2O_3, respectively. In constructing a tight-binding model, we aim to describe the above key features of the DFT band structure.

III. TIGHT-BINDING MODEL

A. Model derivation

We derive Wannier functions from the DFT band structure using Wannier90[40] to construct the tight-binding basis. Wannier functions are initialized on the Ga(Al) sites with s- and p-orbital symmetry and on the O sites with p-orbital symmetry. We selectively localize only the Ga-s(Al-s) Wannier functions onto Ga(Al) sites using a Lagrange multiplier.[41] Selectively localized Wannier functions improve the localization of Ga-s(Al-s) Wannier functions at the cost of delocalizing Ga-p(Al-p) Wannier functions, which describe the higher conduction bands (>5 eV above the conduction band minimum). We find that the O-p Wannier functions have similar localization in both schemes.

We show isosurface plots of Ga-s Wannier functions in β and α phases resulting from selective localization in Figs. 1(c) and 1(d). (The Al-s and Ga-s Wannier functions in the α phase are qualitatively similar.) The Wannier functions reproduce the distorted tetrahedral and octahedral symmetry of the coordination polyhedra as expected from the hybridization between the Ga-4s and O-2p atomic orbitals in Ga_2O_3.

We construct the tight-binding model from the Wannier function basis by the following procedure:

1. Extract the DFT Hamiltonian matrix element in the Wannier basis.[42]
2. Truncate the couplings to nearest-neighbor (Ga,Al)-O and (Ga,Al)-(Ga,Al) coupling, keeping only the Wannier functions of s-symmetry on the (Ga,Al) basis.
3. The (Ga,Al) site energies and (Ga,Al)-O nearest-neighbor coupling are then scaled to fit to the experimental bandgap and conduction band effective mass.

The parameterization of our tight-binding model takes the following form:

$$\hat{H} = \sum_i \varepsilon_i |i\rangle\langle i| + \sum_{i,j} t_{ij} e^{-i\vec{k}\cdot\Delta\vec{d}_{ij}} |j\rangle\langle i| + c.c. \quad (1)$$

The right-hand side of the first line describes the contribution of individual Wannier functions to the total energy, commonly called

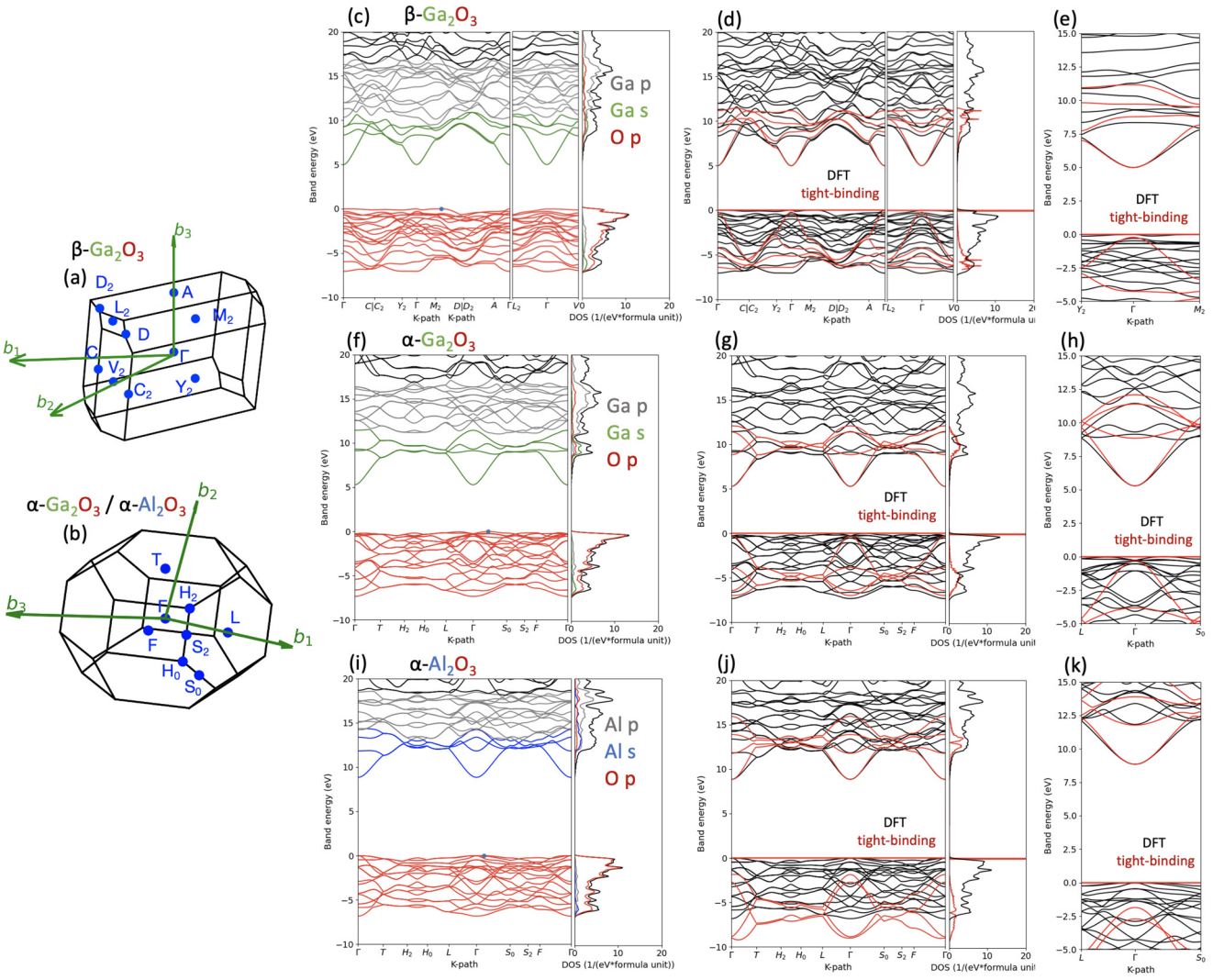

FIG. 2. Electronic structure of β-Ga_2O_3, α-Ga_2O_3, and α-Al_2O_3. (a) and (b) The first Brillouin zone of the monoclinic β and rhombohedral α phases. (c), (f), and (i) The DFT band structure and orbital-projected DOS of β-Ga_2O_3, α-Ga_2O_3, and α-Al_2O_3. The DFT bandgaps have been tuned to the experimental bandgaps via a scissor cut. Color coordination indicates the orbital character of the bands and projected DOS. The blue dots indicate the valence band maximum. (d), (g), and (j) The tight-binding band structure and DOS (red) plotted over the DFT data (black). The sharp peak in the tight-binding DOS at the top of the valence band is due to the lack of O-p to O-p coupling in the tight-binding model. (e), (h), and (k) DFT (black) and tight-binding (red) band structure near the Γ point. The reciprocal space vectors and high-symmetry points are given in Table III.

the on-site energy. The second line describes the kinetic energy of the electrons, commonly called the "hopping" energy. In Eq. (1), $|i\rangle$ represents the ith Wannier function with on-site energy ε_i. $t_{ij} = \tilde{t}_{ij}e^{i\phi_{ij}}$ is the hopping term between ith and jth Wannier functions. Here, ϕ_{ij} characterizes the phase of t_{ij} and encompasses the symmetry of the local bonding environment. $\vec{k}$ is the wavevector, and $\Delta\vec{d}_{ij}$ is the displacement vector of the two Wannier functions i and j defined as $\Delta\vec{d}_{ij} = \vec{d}_j - \vec{d}_i + \vec{R}$. Here, $\vec{d}_i$ and $\vec{d}_j$ are the centers of Wannier function i and j within the same unit cell, and $\vec{R}$ is the unit cell translation to indicate coupling across adjacent unit cells. The spectrum and wavefunctions are found by solving $\hat{H}\psi = E\psi$.

In our tight-binding model, we include only the s-orbital-derived Wannier functions from the 4 Ga(Al) atoms and the 3 p-orbital-derived Wannier functions from the 6 O atoms. This translates to a 22×22 matrix when the model is implemented numerically. To describe the band structure with a minimal set of parameters, we include (1) the on-site energy ε_i terms for Ga-s(Al-s) and O-p, (2) the nearest-neighbor Ga-s(Al-s) to O-p, and (3) the dominant Ga-s(Al-s) to Ga-s(Al-s) terms (t_{ij}). This amounts to a nearest-neighbor tight-binding model augmented by the Ga-s(Al-s) to Ga-s (Al-s) next-nearest-neighbor hopping. These next-nearest-neighbor terms aid in the accuracy of the higher Ga-4s(Al-3s) derived

conduction bands. With these simplifications, the model contains 60 parameters depending on the structural phases (see Tables IV–VI in the Appendix). Including the Ga-p(Al-p) Wannier functions and O-p to O-p coupling terms gives a satisfactory description of valence band DOS at the cost of significantly increasing the number of parameters (around 300 terms) but provides little improvement to the description of the lower conduction bands. Thus, we neglect these terms in our model.

To reproduce the experimental bandgaps and conduction band effective masses, we adjust the Ga-s(Al-s) on-site energy and tune the Ga-s(Al-s) to O-p coupling term. (We note that in their model of β-Ga_2O_3, Lee *et al.*[19] focus on surface and defect formation energies, which depend on the broad features of the band structure. As a result, their tight-binding model overestimates the conduction band effective mass.) The lists of parameters are given in Table IV, V, and VI and have been implemented in a short program in the supplementary material for convenience.

B. Model Hamiltonian at the Γ point

When implementing the tight-binding model on a computer, Eq. (1) can be written as a 22×22 matrix defined on the basis of 4 Ga-s(Al-s) and 18 O-p Wannier functions. In evaluating the model, the on-site energy ε_i becomes diagonal terms, while the hopping terms t_{ij} populate the ith row and jth column and must be multiplied by the phase factor $e^{-i\vec{k}\cdot\Delta\vec{d}_{ij}}$ at each k-point. To illustrate the model and gain insight into the material physics, we explicitly evaluate the tight-binding model of β-Ga_2O_3 at the Γ-point ($\vec{k} = \vec{0}$). We find that the tight-binding model at the Γ-point can be written in the block-matrix form,

$$H = \begin{pmatrix} H_{Ga:s} & H^{\dagger}_{Ga:s,O:p_x} & 0 & H^{\dagger}_{Ga:s,O:p_z} \\ H_{Ga:s,O:p_x} & H_{O:p_x} & 0 & 0 \\ 0 & 0 & H_{O:p_y} & 0 \\ H_{Ga:s,O:p_z} & 0 & 0 & H_{O:p_z} \end{pmatrix}, \quad (2)$$

where $H_{Ga:s}$, $H_{O:p_x}$, $H_{O:p_y}$, and $H_{O:p_z}$ blocks define the coupling within the Ga-s, O-p_x, O-p_y, and O-p_z Wannier function sub-spaces, respectively. The $H_{Ga:s,O:p_x}$ and $H_{Ga:s,O:p_z}$ blocks describe the coupling between the Ga-s, O-p_x, and O-p_z Wannier functions, respectively. We construct the tight-binding model so that it reflects the crystal symmetry. This can be seen clearly in the lack of coupling between the Ga-s and O-p_y Wannier functions. The twofold rotation about the crystallographic b-axis and the mirror operation through the plane perpendicular to the b-axis guarantee that this coupling is zero at the Γ-point. The coupling between different O-p Wannier function blocks (e.g., O-p_x and O-p_y) is zero because we have neglected the coupling within the valence band. At the Γ point, the phase factor $e^{-i\vec{k}\cdot\Delta\vec{d}_{ij}} \to 1$, leaving the matrix real and symmetric.

$H_{Ga:s}$ takes the form

$$H_{Ga:s} = \begin{pmatrix} \varepsilon_{Ga1:s} + 2t_{Ga1:s,Ga1:s} & 0 & 0 & 0 \\ 0 & \varepsilon_{Ga1:s} + 2t_{Ga1:s,Ga1:s} & 0 & 0 \\ 0 & 0 & \varepsilon_{Ga3:s} + 2t_{Ga3:s,Ga3:s} & t_{Ga3:s,Ga4:s} \\ 0 & 0 & t_{Ga3:s,Ga4:s} & \varepsilon_{Ga3:s} + 2t_{Ga3:s,Ga3:s} \end{pmatrix} \to \begin{pmatrix} -7.498 & 00 & 0 \\ 0 & -7.498 & 00 \\ 0 & 0-7.222 & 0.216 \\ 0 & 00.216 & -7.222 \end{pmatrix}, \quad (3)$$

which is written on the basis $(|Ga1:s\rangle, |Ga2:s\rangle, |Ga3:s\rangle, |Ga4:s\rangle)$ of Ga-s Wannier functions. Taking values from Table IV, we have included the numerical value of the block in eV. Since Ga1:s and Ga2:s are equivalent tetrahedral sites while Ga3:s and Ga4:s are equivalent octahedral sites, each has the same on-site energy and coupling. Notice that on-site energies $\varepsilon_{Ga:1s}$ and $\varepsilon_{Ga:3s}$ are modified by coupling to the same Ga sites in the neighboring unit cells ($t_{Ga1:s,Ga1:s}$ and $t_{Ga3:s,Ga3:s}$). Furthermore, the octahedral sites are weakly coupled with each other.

In simplifying the description of the valence band, we neglect the coupling between O-p Wannier functions. As a result, each $H_{O:px}$, $H_{O:py}$, and $H_{O:pz}$ block is diagonal and can be written as

$$H_{O:px} = H_{O:py} = H_{O:pz} = \varepsilon_{O:p} \times \mathbb{I}_{6\times6} \to -12 \times \mathbb{I}_{6\times6}, \quad (4)$$

which is written on the basis $(|O1:p_l\rangle, |O2:p_l\rangle, |O3:p_l\rangle, |O4:p_l\rangle, |O5:p_l\rangle, |O6:p_l\rangle)$ of O-p Wannier functions where $l = x, y, z$. Here, $\mathbb{I}_{6\times6}$ is the 6×6 identity matrix.

The coupling between Ga-s and O-p_x and O-p_z is described by $H_{Ga:s,O:px}$ and $H_{Ga:s,O:pz}$, which evaluates to (hopping strengths connected by symmetries are shown with the same symbol)

$$H_{Ga:s,O:px} = \begin{pmatrix} t_{Ga1:s,O1:px} & 0 & 2t_{Ga3:s,O1:px} & 0 \\ 0 & -t_{Ga1:s,O1:px} & 0 & 2t_{Ga4:s,O2:px} \\ t_{Ga1:s,O3:px} & 0 & 0 & -t_{Ga3:s,O4:px} \\ 0 & t_{Ga2:s,O4:px} & t_{Ga3:s,O4:px} & 0 \\ 0 & -2t_{Ga1:s,O6:px} & t_{Ga3:s,O5:px} & 0 \\ 2t_{Ga1:s,O6:px} & 0 & 0 & -t_{Ga3:s,O5:px} \end{pmatrix} \to \begin{pmatrix} 0.651 & 0 & 0.710 & 0 \\ 0 & -0.651 & 0 & -0.703 \\ 2.592 & 0 & 0 & -2.877 \\ 0 & -2.595 & 2.877 & 0 \\ 0 & 3.499 & -2.965 & 0 \\ -3.496 & 0 & 0 & 2.965 \end{pmatrix}, \quad (5)$$

$$H_{Ga:s,O:pz} = \begin{pmatrix} t_{Ga1:s,O1:pz} & 0 & 2t_{Ga3:s,O1:pz} & 0 \\ 0 & -t_{Ga1:s,O1:pz} & 0 & 2t_{Ga4:s,O2:pz} \\ t_{Ga1:s,O3:px} & 0 & 2t_{Ga3:s,O3:pz} & -t_{Ga3:s,O4:pz} \\ 0 & -t_{Ga2:s,O4:px} & t_{Ga3:s,O4:pz} & -2t_{Ga4:s,O4:pz} \\ 0 & -2t_{Ga1:s,O6:pz} & t_{Ga3:s,O5:pz} & 0 \\ 2t_{Ga1:s,O6:pz} & 0 & 0 & -t_{Ga3:s,O5:pz} \end{pmatrix} \rightarrow \begin{pmatrix} 3.466 & 0 & -3.307 & 0 \\ 0 & -3.466 & 0 & 3.314 \\ 2.592 & 0 & 3.345 & -1.101 \\ 0 & 2.595 & 1.101 & -3.326 \\ 0 & 0.885 & -0.621 & 0 \\ -0.880 & 0 & 0 & 0.621 \end{pmatrix}. \quad (6)$$

Here, terms appear as pairs with opposite signs, manifesting the twofold symmetry of the monoclinic structure. $H_{Ga:s,O:px}$ and $H_{Ga:s,O:pz}$ look formally similar but are not exactly the same. Again, the matrix coupling Ga-s to O-py vanishes at the Γ point but will show up away from it. The complete set of matrix elements can be found in Table IV. The eigenvalues of the 22 × 22 matrix correspond to the energy eigenstates at the given k-point, and the eigenvectors correspond to the wavefunctions. To generate the band structure, one generates the matrix at sampled k-points along the path and solve for the eigenvalues. The complexity of numerical eigensolvers depends on the matrix dimension as $O(n^3)$. As a comparison, our DFT calculation relies on around 5000 planar waves as a basis; therefore, the tight-binding model provides a significant speedup. In our experience, a tight-binding band structure can be generated on a personal computer in seconds.

C. Comparison between tight-binding and the DFT band structure

Figures 2(d), 2(g), and 2(j) show the tight-binding band structure and DOS superimposed on the DFT results. In all three phases, the experimental bandgaps and conduction band effective masses are reproduced by the adjustment of parameters mentioned above. Moreover, the tight-binding model gives a satisfactory description of the parabolic to linear dispersion, the second conduction band at the Γ point, and the flat valence band edge states.

The slope of the linear dispersion of the lowest conduction band away from Γ and the energy of the second conduction band at Γ are slightly overestimated due to the absence of interaction from higher Ga-p(Al-p) bands. This phenomenon is well-known in the tight-binding description of Si, Ge, and III–V semiconductors[43] where it is due to the lack of interactions from higher energy bands. The lack of O-p to O-p coupling leaves some of the O-p states non-dispersive. As a result, the tight-binding model cannot describe the small difference between the valence band at Γ and the DFT predicted valence band maximum between Γ and T in the β phase and Γ and S_0 in the α phases. This leaves a large peak in the DOS at the valence band edge [see Figs. 2(d), 2(g), and 2(j)], which could be resolved in future models that include O-p to O-p coupling.

D. α-Ga_2O_3/α-Al_2O_3 [0001] superlattices

We now apply the tight-binding model described above to superlattices of Ga_2O_3 and Al_2O_3 in the α-phase. The superlattice is constructed by interfacing layers of conventional (hexagonal) cells of α-Ga_2O_3 and α-Al_2O_3 along the [0001] direction through the shared O plane so that the octahedral (Ga,Al)-O environment is preserved. Figure 3(a) shows the superlattice crystal structure with one hexagonal cell of Ga_2O_3 and one hexagonal cell of Al_2O_3. The hexagonal cell is transformed from the primitive (rhombohedral) cell by the following transformation:

$$\begin{pmatrix} \vec{a}_h \\ \vec{b}_h \\ \vec{c}_h \end{pmatrix} = \begin{pmatrix} -1 & 1 & 0 \\ 1 & 0 & -1 \\ 1 & 1 & 1 \end{pmatrix} \begin{pmatrix} \vec{a}_r \\ \vec{b}_r \\ \vec{c}_r \end{pmatrix}, \quad (7)$$

where $\left(\vec{a}_h, \vec{b}_h, \vec{c}_h\right)$ and $\left(\vec{a}_r, \vec{b}_r, \vec{c}_r\right)$ are the hexagonal and rhombohedral lattice constant, respectively.

To simplify the application of the tight-binding model to the Ga_2O_3/Al_2O_3 superlattice, we set all lattice constants to those of α-Al_2O_3 and leave the fractional internal coordinates at their bulk values. We apply the tight-binding model of (1) and Tables V and VI. Inside the Ga_2O_3/Al_2O_3 region, the tight-binding description is constructed in the same way as the bulk by including the nearest-neighbor (Ga,Al)-O couplings and next nearest-neighbor (Ga, Al)–(Ga,Al) couplings. The tight-binding interaction at the interface is accomplished by hopping through the shared O atoms via $t_{Ga,O}$ and $t_{Al,O}$ and a parallel channel, which directly couples the Ga to Al, $t_{Ga,Al} = \frac{t_{Ga,Ga}+t_{Al,Al}}{2}$ [see Fig. 3(a), inset].

We explore two strategies to study the quantum confinement of the bands [Fig. 3(b)]: (1) fixing the thickness of Ga_2O_3 layers to one hexagonal cell and varying the number of the Al_2O_3 hexagonal cells (upper panel) and (2) simultaneously varying the thickness of the Ga_2O_3 layers and Al_2O_3 layers (lower panel).

The band structure of the superlattice with one conventional cell of Ga_2O_3 and one conventional cell of Al_2O_3 is presented in Fig. 3(c), following the high-symmetry path in the hexagonal Brillouin zone. The valence band maxima of Ga_2O_3 and Al_2O_3, both O-derived, are aligned under the tight-binding approximation, which is consistent with recent DFT calculations.[44] Moving up in energy from the valence band, the Ga-derived supercell conduction band minima appear at ≈6 eV. The Al-derived bands do not appear until ≈9 eV, as expected from the bandgap differences of the two materials [see Fig. 3(b)]. Due to the increase in the periodic length along the c-axis in the supercell, we observe zone-folding along the Γ-path. This gives rise to nearly flat minibands, suggesting that the states in each Ga_2O_3 quantum well are weakly coupled

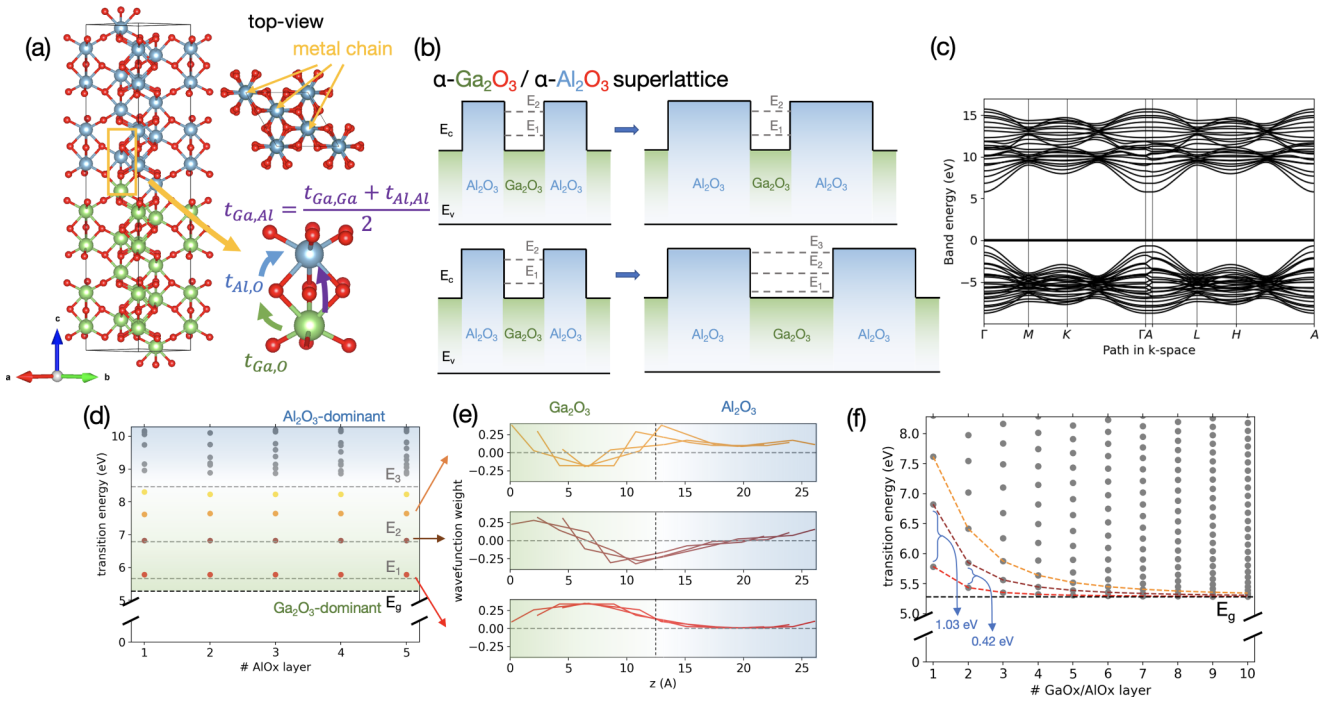

FIG. 3. Crystal and electronic structure of α-Ga_2O_3/α-Al_2O_3 superlattices along the [0001] direction. (a) The superlattice is constructed by interfacing conventional (hexagonal) cells of Ga_2O_3 and Al_2O_3 along the [0001] direction. The effective hopping across the interface is shown in the inset. (b) Flatband diagram of the superlattice quantum confinement of fixed Ga_2O_3 for varied Al_2O_3 thicknesses (upper) and varied Ga_2O_3 and Al_2O_3 thicknesses (lower). (c) Superlattice band structure from the tight-binding model for one conventional cell of Ga_2O_3 and one conventional cell of Al_2O_3. (d) Transition energy from the valence band edge to the conduction subbands from the tight-binding model for fixed Ga_2O_3 thickness [upper panel of (b)]. The dashed lines are calculated from the finite-well model. (e) Eigenvectors of the lowest three conduction subbands projected onto the metal sites showing the expected even (bottom), odd (middle), and even (top) parity in the confined Ga_2O_3 region (shaded green). The vertical dashed line represents the interface between Ga_2O_3 (green shaded region—left) and Al_2O_3 (blue shaded region—right). (f) Transition energy from the valence band edge to the conduction subbands from the tight-binding model for varied Ga_2O_3 thicknesses [lower panel of (b)]. The first three transition energies have been color coordinated with (d) by the guide line. The lowest intersubband transition energies are shown for single and double cell Ga_2O_3/Al_2O_3.

with each other. Because the hexagonal cell is three times the volume of the rhombohedral cell, more bands appear in the superlattice band structure than the bulk band structure.

We now schematically investigate the major optical transitions expected from the tight-binding construction. Figure 3(d) shows the transition energy from the valence band edge to the conduction subbands at the Γ point from Fig. 3(c). The tight-binding model reveals four bound states inside the Ga_2O_3 quantum well [shaded green in Fig. 3(d)]. A dense manifold of free states appears above these four bound states with wavefunctions dominated by the higher conduction subbands of Ga_2O_3 and the Al_2O_3 conduction bands [shaded blue in Fig. 3(d)].

As the thickness of the Al_2O_3 layer is increased, the bound states are only weakly perturbed, whereas the free states approach a continuum. The insensitivity of the bound Ga_2O_3 transition energies to Al_2O_3 thickness is due to the large starting thickness (1.3 nm) of the Al_2O_3 hexagonal cell, rendering the coupling between adjacent Ga_2O_3 quantum wells weak even in the single conventional Al_2O_3 layer limit. We find that the typical energy change in the bound states with increasing Al_2O_3 thickness is on the order of 10 meV, which is not discernible on the plot.

We compare the Γ point transition energies with a numerical calculation of the bound states in the finite quantum well with a barrier height of 3.6 eV (from the Ga_2O_3/Al_2O_3 band alignment), the effective mass of Ga_2O_3 (0.33 m_e) and Al_2O_3 (0.44 m_e), and the width of the Ga_2O_3 well (1.31 nm). We solve the 1D Schrödinger equation using the finite element method for a single quantum well with a central Ga_2O_3 region surrounded by extended Al_2O_3 regions, with parabolic bands, solving for the eigenenergies. The transition energies from the numerical calculations of the finite quantum well are shown as the gray lines in Fig. 3(d). The lowest state is energetically higher than the conduction band minimum (black dashed line) due to quantum confinement. Reasonable agreement is found with the first two states of the tight-binding model. While the tight-binding model predicts four

bound states, the quantum well calculation predicts only three. We attribute this difference to the non-parabolicity of the higher energy Ga_2O_3 conduction band and the breakdown of the square-well potential approximation.

Figure 3(e) shows the first three eigenvectors ψ representing confined states from the tight-binding Hamiltonian for a single Ga_2O_3 and a single Al_2O_3 hexagonal cell, projected onto the three inequivalent metal chains shown in the top-view of Fig. 3(a). All three states are centered in the Ga_2O_3 region with weakly evanescent tails penetrating into the Al_2O_3 region, manifesting their bound state nature. The lowest energy state has zero nodes, the second state has one node, and the third state has two nodes [lower, middle, and upper panel of Fig. 3(e)]. Such parities suggest that optical transition from the first to the second states and from the second to the third states are allowed for radiation polarized along the superlattice direction.

This inter-subband transition energy can be controlled by changing the thickness of Ga_2O_3 and Al_2O_3, shown in Fig. 3(f). With weaker quantum confinement at increasing thickness, the offset of the lowest state from the conduction band minimum diminishes, and the inter-subband transition energies decrease. For a single hexagonal cell of Ga_2O_3, the inter-subband transition energy is 1.03 eV, while for two hexagonal cells of Ga_2O_3, the inter-subband transition energy is 0.41 eV, spanning the technologically relevant wavelength of 1.55 μm (0.8 eV). This suggests that engineering supercells of Ga_2O_3 and Al_2O_3, with Ga_2O_3 thickness between one and two hexagonal layers, provides a novel design space for photonics devices applicable to telecommunications.

IV. CONCLUSION

We have derived a minimal tight-binding model for β-Ga_2O_3, α-Ga_2O_3, and α-Al_2O_3 using selectively localized Wannier functions as a basis. The Wannier functions reflect the local symmetry of the atomic sites and the tight-binding model satisfactorily reproduces the electronic structure throughout the Brillouin zone. By constraining the hopping parameters, we have fit the isotropic conduction band effective mass, suggesting low field transport experiments can be described by the tight-binding model. By including the higher energy Ga-s(Al-s) conduction bands, the tight-binding model can also describe the parabolic to linear dispersion which suggests application to high-field electronic transport as well. Additionally, by reproducing the experimental bandgap, we expect that the tight-binding model can simulate the major features in optical absorption including the primary optical transition from the O-p valence bands to the Ga-s(Al-s) conduction bands, and the optical transition from the valence band to the higher energy conduction bands. In future work, this model can be extended to describe chemical and mechanical properties,[45,46] which will address additional hurdles in material investigation and device designs.

Finally, by applying the tight-binding model to α-Ga_2O_3/α-Al_2O_3 superlattices along the [0001] direction, we predict inter-subband transitions that can be engineered to span the 1.55 μm telecommunications window. Comparing this material system with conventional narrow bandgap semiconductors, the wide bandgap of the host materials (5.2–8.8 eV) allows for clean inter-subband transitions, absent of bulk interband effects that may impede photonic device design and operation. Additionally, the large barrier height (3.6 eV) provides flexible design of inter-subband transitions that may be only weakly coupled to other higher-order transitions. These two realizations, when merged, open new avenues for oxide photonics. We expect the tight-binding models to aid in the description and development of electronic and optical devices utilizing bulk, nanostructured, heterostructured, and strained variants of β-Ga_2O_3, α-Ga_2O_3, and α-Al_2O_3.

SUPPLEMENTARY MATERIAL

See the supplementary material for tight-binding model parameters in text files and sample Python programs for constructing the tight-binding band structure.

ACKNOWLEDGMENTS

Y.Z. and G.K. would like to thank Jeffrey Kaaret for his help with the comparison of our model to other tight-binding programs. This research project was conducted using computational resources at the Maryland Advanced Research Computing Center (MARCC) and was supported by the National Science Foundation [Platform for the Accelerated Realization, Analysis, and Discovery of Interface Materials (PARADIM)] under Cooperative Agreement No. DMR-1539918.

AUTHOR DECLARATIONS

Conflict of Interest

The authors have no conflicts to disclose.

DATA AVAILABILITY

The data that support the findings of this study are available within the article and its supplementary material.

APPENDIX: TIGHT-BINDING PARAMETERS

In the Appendix, we include additional information for the tight-binding models of the monoclinic β-Ga_2O_3 and the rhombohedral α-Ga_2O_3 and α-Al_2O_3 phases. Table II gives the structural information from density functional theory in scaled coordinates. Table III shows the high-symmetry points in reciprocal space for the monoclinic and rhombohedral structures. Tables IV–VI give the explicit tight-binding models for each phase. The tight-binding basis functions are Wannier functions centered on the specified sites with the specified symmetry. For example, "Ga2 s" represents a Wannier function centered on the second Ga site with s-orbital symmetry.

TABLE II. Structural parameters of β-Ga_2O_3, α-Ga_2O_3, and α-Al_2O_3. The Cartesian coordinate of a site i is given by $\vec{d}_i = A_1\vec{a_1} + A_2\vec{a_2} + A_3\vec{a_3}$.

Lattice	β-Ga_2O_3			Lattice	α-Ga_2O_3			Lattice	α-Al_2O_3		
vector (Å)	x	y	z	vector (Å)	x	y	z	vector (Å)	x	y	z
$\vec{a_1}$	6.115	1.620	0.000	$\vec{a_1}$	2.491	1.438	4.478	$\vec{a_1}$	2.403	1.387	4.372
$\vec{a_2}$	−6.115	1.620	0.000	$\vec{a_2}$	−2.491	1.438	4.478	$\vec{a_2}$	−2.403	1.387	4.372
$\vec{a_3}$	−1.374	0.000	5.635	$\vec{a_3}$	0.000	−2.877	4.478	$\vec{a_3}$	0.000	−2.774	44.372
Site				Site				Site			
coordinate	A_1	A_2	A_3	coordinate	A_1	A_2	A_3	coordinate	A_1	A_2	A_3
Ga1	0.090	−0.090	0.795	Ga1	0.179	0.179	0.179	Al1	0.818	−0.162	−0.177
Ga2	0.910	0.090	0.205	Ga2	0.678	0.678	−0.322	Al2	0.671	0.659	−0.311
Ga3	0.659	0.341	0.314	Ga3	0.821	−0.179	−0.179	Al3	0.330	0.318	−0.664
Ga4	0.341	−0.341	0.686	Ga4	0.322	0.322	−0.678	Al4	0.174	0.182	0.164
O1	0.165	−0.165	0.109	O1	0.553	−0.053	0.250	O1	0.750	−0.558	0.057
O2	0.835	0.165	0.891	O2	0.941	0.250	−0.441	O2	0.942	0.250	−0.442
O3	0.173	−0.173	0.563	O3	0.250	0.559	−0.059	O3	1.058	−0.250	−0.558
O4	0.827	0.173	0.437	O4	1.059	−0.250	−0.559	O4	0.442	0.058	−0.250
O5	0.496	−0.496	0.256	O5	0.750	−0.559	0.059	O5	0.558	−0.058	0.250
O6	0.504	0.496	0.743	O6	0.441	0.059	−0.250	O6	0.250	0.558	−0.058

TABLE III. High-symmetry points in the first Brillouin zone of the β and α phase. Coordinates are calculated by $\vec{k} = B_1\vec{b_1} + B_2\vec{b_2} + B_3\vec{b_3}$, in which $\vec{b_1}$, $\vec{b_2}$, and $\vec{b_3}$ are the reciprocal lattice vector. $\vec{b_1}$, $\vec{b_2}$, and $\vec{b_3}$ can be calculated by $(\vec{b_1}\vec{b_2}\vec{b_3}) = ((\vec{a_1}\vec{a_2}\vec{a_3})^{-1})^T$.

	β phase		
	B_1	B_2	B_3
Γ	0.0000	0.0000	0.0000
C	0.2662	0.2662	0.0000
C_2	−0.2662	0.7338	0.0000
Y_2	−0.5000	0.5000	0.0000
M_2	−0.5000	0.5000	0.5000
D	−0.2580	0.7419	0.5000
D_2	0.2580	0.2580	0.0000
A	0.0000	0.0000	0.5000
L_2	0.0000	0.5000	0.5000
V_2	0.0000	0.5000	0.0000
	α phase		
	B_1	B_2	B_3
Γ	0.0000	0.0000	0.0000
T	0.5000	0.5000	0.5000
H_2	0.7641	0.2358	0.5000
H_0	0.5000	−0.2358	0.2358
L	0.5000	0.0000	0.0000
S_0	0.3679	−0.3679	0.0000
S_2	0.6320	0.0000	0.3679
F	0.5000	0.0000	0.5000

TABLE IV. Tight-binding parameters of β-Ga_2O_3. $\vec{R}$ is written in integer multiples of lattice vectors [ijk] and can be translated to Cartesian coordinates by $\vec{R} = i\vec{a_1} + j\vec{a_2} + k\vec{a_3}$, where a_1, a_2, and a_3 are the lattice vectors. The hopping parameters describe hopping from atom centered Wannier functions with s- or p-symmetry.

On-site energy

Site i	ε_i (eV)
Ga1, Ga2	4.95
Ga3, Ga4	4.52
All O	0

Hopping parameters

Site i	Site j	$\vec{R}$	$\tilde{t}_{ij}$ (eV)	ϕ_{ij}
Ga1 s	Ga1 s	[1, 1, 0]	0.224	π
Ga2 s	Ga2 s	[1, 1, 0]	0.224	π
Ga3 s	Ga3 s	[1, 1, 0]	0.129	0
Ga3 s	Ga4 s	[0, 0, 0]	0.108	0
Ga3 s	Ga4 s	[1, 1, 0]	0.108	0
Ga4 s	Ga4 s	[1, 1, 0]	0.129	0
Ga1 s	O1 px	[0, 0, 1]	0.652	0
Ga1 s	O1 pz	[0, 0, 1]	3.467	0
Ga1 s	O3 px	[0, 0, 0]	2.592	0
Ga1 s	O3 pz	[0, 0, 0]	2.592	π
Ga1 s	O6 px	[0, 0, 0]	1.748	π
Ga1 s	O6 px	[−1, −1, 0]	1.748	π

TABLE IV. (*Continued.*)

On-site energy

Site i	ε_i (eV)
Ga1, Ga2	4.95
Ga3, Ga4	4.52
All O	0

Hopping parameters

Site i	Site j	$\vec{R}$	$\tilde{t}_{ij}$ (eV)	ϕ_{ij}
Ga1 s	O6 py	[0, 0, 0]	3.029	0
Ga1 s	O6 py	[− 1, − 1, 0]	3.029	π
Ga1 s	O6 pz	[0, 0, 0]	0.440	π
Ga1 s	O6 pz	[− 1, − 1, 0]	0.440	π
Ga2 s	O2 px	[0, 0, − 1]	0.652	π
Ga2 s	O2 pz	[0, 0, − 1]	3.467	π
Ga2 s	O4 px	[0, 0, 0]	2.596	π
Ga2 s	O4 pz	[0, 0, 0]	2.596	0
Ga2 s	O5 px	[0, 0, 0]	1.750	0
Ga2 s	O5 px	[1, 1, 0]	1.750	0
Ga2 s	O5 py	[0, 0, 0]	3.030	π
Ga2 s	O5 py	[1, 1, 0]	3.030	0
Ga2 s	O5 pz	[0, 0, 0]	0.443	0
Ga2 s	O5 pz	[1, 1, 0]	0.443	0
Ga3 s	O1 px	[0, 0, 0]	0.355	0
Ga3 s	O1 px	[1, 1, 0]	0.355	0
Ga3 s	O1 py	[0, 0, 0]	2.484	π
Ga3 s	O1 py	[1, 1, 0]	2.484	0
Ga3 s	O1 pz	[0, 0, 0]	1.654	π
Ga3 s	O1 pz	[1, 1, 0]	1.654	π
Ga3 s	O3 py	[0, 0, 0]	2.162	π
Ga3 s	O3 py	[1, 1, 0]	2.162	0
Ga3 s	O3 pz	[0, 0, 0]	1.673	0
Ga3 s	O3 pz	[1, 1, 0]	1.673	0
Ga3 s	O4 px	[0, 0, 0]	2.878	0
Ga3 s	O4 pz	[0, 0, 0]	1.102	0
Ga3 s	O5 px	[0, 1, 0]	2.965	π
Ga3 s	O5 pz	[0, 1, 0]	0.622	π
Ga4 s	O2 px	[0, 0, 0]	0.352	π
Ga4 s	O2 px	[− 1, − 1, 0]	0.352	π
Ga4 s	O2 py	[0, 0, 0]	2.484	0
Ga4 s	O2 py	[− 1, − 1, 0]	2.484	π
Ga4 s	O2 pz	[0, 0, 0]	1.657	0
Ga4 s	O2 pz	[− 1, − 1, 0]	1.657	0
Ga4 s	O3 px	[0, 0, 0]	2.878	π
Ga4 s	O3 pz	[0, 0, 0]	1.102	π
Ga4 s	O4 py	[0, 0, 0]	2.164	0
Ga4 s	O4 py	[− 1, − 1, 0]	2.164	π
Ga4 s	O4 pz	[0, 0, 0]	1.663	π
Ga4 s	O4 pz	[− 1, − 1, 0]	1.663	π
Ga4 s	O6 px	[0, − 1, 0]	2.965	0
Ga4 s	O6 pz	[0, − 1, 0]	0.622	0

TABLE V. Tight-binding parameters of α-Ga_2O_3. $\vec{R}$ is written in integer multiples of lattice vectors [*ijk*] and can be translated to Cartesian coordinates by $\vec{R} = i\vec{a_1} + j\vec{a_2} + k\vec{a_3}$, where a_1, a_2, and a_3 are the lattice vectors. The hopping parameters describe hopping from atom centered Wannier functions with s- or p-symmetry.

On-site energy

Site i	ε_i (eV)
All Ga	−5.48
All O	−10.5

Hopping parameters

Site i	Site j	$\vec{R}$	$\tilde{t}_{ij}$	ϕ_{ij}
Ga1 s	Ga3 s	[0, 0, 0]	0.012	0
Ga1 s	Ga3 s	[− 1, 1, 0]	0.013	0
Ga1 s	Ga3 s	[− 1, 0, 1]	0.013	0
Ga1 s	Ga4 s	[0, 0, 1]	0.014	π
Ga1 s	Ga4 s	[0, − 1, 1]	0.010	π
Ga1 s	Ga4 s	[− 1, 0, 1]	0.010	π
Ga2 s	Ga3 s	[0, 0, 0]	0.010	π
Ga2 s	Ga3 s	[0, 1, 0]	0.014	π
Ga2 s	Ga3 s	[− 1, 1, 0]	0.010	π
Ga2 s	Ga4 s	[0, 0, 1]	0.013	0
Ga2 s	Ga4 s	[0, 1, 0]	0.013	0
Ga2 s	Ga4 s	[1, 0, 0]	0.013	0
Ga1 s	O1 px	[0, 0, 0]	1.983	0
Ga1 s	O1 py	[0, 0, 0]	0.105	0
Ga1 s	O1 pz	[0, 0, 0]	1.860	0
Ga1 s	O2 px	[− 1, 0, 1]	0.910	π
Ga1 s	O2 py	[− 1, 0, 1]	1.766	π
Ga1 s	O2 pz	[− 1, 0, 1]	1.864	0
Ga1 s	O3 px	[0, 0, 0]	1.076	π
Ga1 s	O3 py	[0, 0, 0]	1.673	0
Ga1 s	O3 pz	[0, 0, 0]	1.867	0
Ga1 s	O4 px	[− 1, 0, 1]	1.151	0
Ga1 s	O4 py	[− 1, 0, 1]	2.402	π
Ga1 s	O4 pz	[− 1, 0, 1]	1.248	π
Ga1 s	O5 px	[− 1, 1, 0]	2.654	π
Ga1 s	O5 py	[− 1, 1, 0]	0.216	0
Ga1 s	O5 pz	[− 1, 1, 0]	1.246	π
Ga1 s	O6 px	[0, 0, 0]	1.509	0
Ga1 s	O6 py	[0, 0, 0]	2.197	0
Ga1 s	O6 pz	[0, 0, 0]	1.242	π
Ga2 s	O1 px	[0, 1, − 1]	1.511	π
Ga2 s	O1 py	[0, 1, − 1]	2.198	0
Ga2 s	O1 pz	[0, 1, − 1]	1.249	π
Ga2 s	O2 px	[0, 0, 0]	2.656	0
Ga2 s	O2 py	[0, 0, 0]	0.216	0
Ga2 s	O2 pz	[0, 0, 0]	1.242	π
Ga2 s	O3 px	[0, 0, 0]	1.142	π
Ga2 s	O3 py	[0, 0, 0]	2.404	π
Ga2 s	O3 pz	[0, 0, 0]	1.245	π
Ga2 s	O4 px	[0, 1, 0]	1.074	0

TABLE V. (*Continued.*)

On-site energy	
Site i	ε_i (eV)
All Ga	−5.48
All O	−10.5

Hopping parameters

Site i	Site j	$\vec{R}$	$\tilde{t}_{ij}$	ϕ_{ij}
Ga2 s	O4 py	[0, 1, 0]	1.664	0
Ga2 s	O4 pz	[0, 1, 0]	1.866	0
Ga2 s	O5 px	[0, 1, 0]	0.904	0
Ga2 s	O5 py	[0, 1, 0]	1.759	π
Ga2 s	O5 pz	[0, 1, 0]	1.872	0
Ga2 s	O6 px	[0, 1, 0]	1.980	π
Ga2 s	O6 py	[0, 1, 0]	0.096	0
Ga2 s	O6 pz	[0, 1, 0]	1.870	0
Ga3 s	O1 px	[0, 0, 0]	1.508	π
Ga3 s	O1 py	[0, 0, 0]	2.191	π
Ga3 s	O1 pz	[0, 0, 0]	1.252	0
Ga3 s	O2 px	[0, 0, 0]	1.151	π
Ga3 s	O2 py	[0, 0, 0]	2.402	0
Ga3 s	O2 pz	[0, 0, 0]	1.251	0
Ga3 s	O3 px	[1, − 1, 0]	2.656	0
Ga3 s	O3 py	[1, − 1, 0]	0.199	π
Ga3 s	O3 pz	[1, − 1, 0]	1.253	0
Ga3 s	O4 px	[0, 0, 0]	0.910	0
Ga3 s	O4 py	[0, 0, 0]	1.779	0
Ga3 s	O4 pz	[0, 0, 0]	1.851	π
Ga3 s	O5 px	[0, 0, 0]	1.084	0
Ga3 s	O5 py	[0, 0, 0]	1.681	π
Ga3 s	O5 pz	[0, 0, 0]	1.853	π
Ga3 s	O6 px	[0, 0, 0]	1.995	π
Ga3 s	O6 py	[0, 0, 0]	0.098	π
Ga3 s	O6 pz	[0, 0, 0]	1.856	π
Ga4 s	O1 px	[0, 0, − 1]	1.989	0
Ga4 s	O1 py	[0, 0, − 1]	0.098	π
Ga4 s	O1 pz	[0, 0, − 1]	1.859	π
Ga4 s	O2 px	[− 1, 0, 0]	1.077	π
Ga4 s	O2 py	[− 1, 0, 0]	1.677	π
Ga4 s	O2 pz	[− 1, 0, 0]	1.862	π
Ga4 s	O3 px	[0, 0, − 1]	0.908	π
Ga4 s	O3 py	[0, 0, − 1]	1.775	0
Ga4 s	O3 pz	[0, 0, − 1]	1.856	π
Ga4 s	O4 px	[− 1, 1, 0]	2.653	π
Ga4 s	O4 py	[− 1, 1, 0]	0.213	π
Ga4 s	O4 pz	[− 1, 1, 0]	1.253	0
Ga4 s	O5 px	[0, 1, − 1]	1.151	0
Ga4 s	O5 py	[0, 1, − 1]	2.405	0
Ga4 s	O5 pz	[0, 1, − 1]	1.249	0
Ga4 s	O6 px	[0, 0, 0]	1.510	0
Ga4 s	O6 py	[0, 0, 0]	2.196	π
Ga4 s	O6 pz	[0, 0, 0]	1.254	0

TABLE VI. Tight-binding parameters of α-Al_2O_3. $\vec{R}$ is written in integer multiples of lattice vectors [ijk] and can be translated to Cartesian coordinates by $\vec{R} = i\vec{a_1} + j\vec{a_2} + k\vec{a_3}$, where a_1, a_2, and a_3 are the lattice vectors. The hopping parameters describe hopping from atom centered Wannier functions with s- or p-symmetry.

On-site energy (eV)	
All Al	7.00
All O	0.00

Hopping parameters

Site i	Site j	$\vec{R}$	$\tilde{t}_{ij}$	ϕ_{ij}
Al1 s	Al2 s	[0, − 1, 0]	1.019	π
Al1 s	Al3 s	[0, 0, 0]	0.429	0
Al1 s	Al3 s	[0, 0, 1]	0.389	0
Al1 s	Al3 s	[1, 0, 0]	0.405	0
Al2 s	Al4 s	[0, 0, 0]	0.406	0
Al2 s	Al4 s	[1, 0, 0]	0.415	0
Al3 s	Al4 s	[0, 0, − 1]	1.024	π
Al1 s	O1 px	[0, 0, 0]	1.592	0
Al1 s	O1 py	[0, 0, 0]	2.614	π
Al1 s	O1 pz	[0, 0, 0]	2.646	π
Al1 s	O2 px	[0, 0, 0]	1.008	π
Al1 s	O2 py	[0, 0, 0]	2.321	0
Al1 s	O2 pz	[0, 0, 0]	1.738	0
Al1 s	O3 px	[0, 0, 0]	1.553	0
Al1 s	O3 py	[0, 0, 0]	2.708	0
Al1 s	O3 pz	[0, 0, 0]	2.685	π
Al1 s	O4 px	[0, 0, 0]	3.249	π
Al1 s	O4 pz	[0, 0, 0]	2.871	π
Al1 s	O5 px	[0, 0, 0]	1.392	π
Al1 s	O5 py	[0, 0, 0]	2.058	π
Al1 s	O5 pz	[0, 0, 0]	1.717	0
Al1 s	O6 px	[1, − 1, 0]	2.352	0
Al1 s	O6 py	[1, − 1, 0]	0.250	π
Al1 s	O6 pz	[1, − 1, 0]	1.597	0
Al2 s	O1 px	[0, 1, 0]	1.578	0
Al2 s	O1 py	[0, 1, 0]	2.783	π
Al2 s	O1 pz	[0, 1, 0]	2.994	0
Al2 s	O2 px	[0, 0, 0]	2.511	0
Al2 s	O2 py	[0, 0, 0]	0.365	0
Al2 s	O2 pz	[0, 0, 0]	1.704	π
Al2 s	O3 px	[0, 1, 0]	1.473	0
Al2 s	O3 py	[0, 1, 0]	2.567	0
Al2 s	O3 pz	[0, 1, 0]	2.657	0
Al2 s	O4 px	[0, 1, 0]	2.998	π
Al2 s	O4 pz	[0, 1, 0]	2.722	0
Al2 s	O5 px	[0, 1, − 1]	1.381	π
Al2 s	O5 py	[0, 1, − 1]	1.901	0
Al2 s	O5 pz	[0, 1, − 1]	1.554	π
Al2 s	O6 px	[0, 0, 0]	1.144	π
Al2 s	O6 py	[0, 0, 0]	2.297	π
Al2 s	O6 pz	[0, 0, 0]	1.769	π
Al3 s	O1 px	[0, 1, − 1]	0.924	0

TABLE VI. (*Continued.*)

On-site energy (eV)	
All Al	7.00
All O	0.00

Hopping parameters

Site i	Site j	$\vec{R}$	$\tilde{t}_{ij}$	ϕ_{ij}
Al3 s	O1 py	[0, 1, − 1]	2.264	0
Al3 s	O1 pz	[0, 1, − 1]	1.620	0
Al3 s	O2 px	[− 1, 0, 0]	1.644	π
Al3 s	O2 py	[− 1, 0, 0]	2.699	π
Al3 s	O2 pz	[− 1, 0, 0]	2.806	π
Al3 s	O3 px	[− 1, 1, 0]	2.385	π
Al3 s	O3 py	[− 1, 1, 0]	0.189	π
Al3 s	O3 pz	[− 1, 1, 0]	1.636	0
Al3 s	O4 px	[0, 0, 0]	1.476	0
Al3 s	O4 py	[0, 0, 0]	2.108	π
Al3 s	O4 pz	[0, 0, 0]	1.798	0
Al3 s	O5 px	[0, 0, − 1]	3.176	0
Al3 s	O5 pz	[0, 0, − 1]	2.857	π
Al3 s	O6 px	[0, 0, − 1]	1.451	π
Al3 s	O6 py	[0, 0, − 1]	2.631	0
Al3 s	O6 pz	[0, 0, − 1]	2.596	π
Al4 s	O1 px	[− 1, 1, 0]	2.510	π
Al4 s	O1 py	[− 1, 1, 0]	0.197	0
Al4 s	O1 pz	[− 1, 1, 0]	1.727	π
Al4 s	O2 px	[− 1, 0, 1]	1.468	π
Al4 s	O2 py	[− 1, 0, 1]	2.660	π
Al4 s	O2 pz	[− 1, 0, 1]	2.715	0
Al4 s	O3 px	[− 1, 0, 1]	0.974	0
Al4 s	O3 py	[− 1, 0, 1]	2.175	π
Al4 s	O3 pz	[− 1, 0, 1]	1.606	π
Al4 s	O4 px	[0, 0, 0]	1.535	0
Al4 s	O4 py	[0, 0, 0]	2.022	0
Al4 s	O4 pz	[0, 0, 0]	1.687	π
Al4 s	O5 px	[0, 0, 0]	3.038	0
Al4 s	O5 pz	[0, 0, 0]	2.702	0
Al4 s	O6 px	[0, 0, 0]	1.619	π
Al4 s	O6 py	[0, 0, 0]	2.746	0
Al4 s	O6 pz	[0, 0, 0]	2.903	0

REFERENCES

[1]M. Higashiwaki, K. Sasaki, A. Kuramata, T. Masui, and S. Yamakoshi, "Gallium oxide (Ga_2O_3) metal-semiconductor field-effect transistors on single-crystal β-Ga_2O_3 (010) substrates," Appl. Phys. Lett. **100**, 013504 (2012).

[2]A. Kuramata, K. Koshi, S. Watanabe, Y. Yamaoka, T. Masui, and S. Yamakoshi, "High-quality β-Ga_2O_3 single crystals grown by edge-defined film-fed growth," Jpn. J. Appl. Phys. **55**, 1202A2 (2016).

[3]D. Gogova, G. Wagner, M. Baldini, M. Schmidbauer, K. Irmscher, R. Schewski, Z. Galazka, M. Albrecht, and R. Fornari, "Structural properties of Si-doped β-Ga_2O_3 layers grown by MOVPE," J. Cryst. Growth **401**, 665–669 (2014).

[4]H. Okumura, M. Kita, K. Sasaki, A. Kuramata, M. Higashiwaki, and J. S. Speck, "Systematic investigation of the growth rate of β-Ga_2O_3 (010) by plasma-assisted molecular beam epitaxy," Appl. Phys. Express **7**, 095501 (2014).

[5]R. Jinno, C. S. Chang, T. Onuma, Y. Cho, S. T. Ho, D. Rowe, M. C. Cao, K. Lee, V. Protasenko, D. G. Schlom, D. A. Muller, H. G. Xing, and D. Jena, "Crystal orientation dictated epitaxy of ultrawide-bandgap 5.4- to 8.6-eV α-$(AlGa)_2O_3$ on m-plane sapphire," Sci. Adv. **7**, eabd5891 (2021).

[6]S. Roy, A. Bhattacharyya, P. Ranga, H. Splawn, J. Leach, and S. Krishnamoorthy, "High-k oxide field-plated vertical (001) β-Ga_2O_3 Schottky barrier diode with Baliga's figure of merit over 1 GW/cm^2," IEEE Electron Device Lett. **42**, 1140–1143 (2021).

[7]N. K. Kalarickal, Z. Xia, H.-l. Huang, W. Moore, Y. Liu, M. Brenner, J. Hwang, and S. Rajan, "β-$(Al_{0.18}Ga_{0.82})_2O_3/Ga_2O_3$ double heterojunction transistor with average field of 5.5 MV/cm," IEEE Electron Device Lett. **42**, 899–902 (2021).

[8]S. J. Pearton, J. Yang, P. H. Cary, F. Ren, J. Kim, M. J. Tadjer, and M. A. Mastro, "A review of Ga_2O_3 materials, processing, and devices," Appl. Phys. Rev. **5**, 011301 (2018).

[9]M. Meneghini, G. Meneghesso, and E. Zanoni, *Power GaN Devices: Materials, Applications and Reliability* (Springer International Publishing, 2017).

[10]W. A. Harrison, *Electronic Structure and the Properties of Solids—The Physics of the Chemical Bond* (Dover Publications, 1989).

[11]S. Datta, *Quantum Transport: Atom to Transistor* (Cambridge University Press, 2005).

[12]R. Lake, G. Klimeck, R. C. Bowen, and D. Jovanovic, "Single and multiband modeling of quantum electron transport through layered semiconductor devices," J. Appl. Phys. **81**, 7845–7869 (1997).

[13]K. Nehari, N. Cavassilas, J. L. Autran, M. Bescond, D. Munteanu, and M. Lannoo, "Influence of band-structure on electron ballistic transport in silicon nanowire MOSFET's: An atomistic study," in *Proceedings of ESSDERC 2005: 35th European Solid-State Device Research Conference* (IEEE, 2005), Vol. 2005, pp. 229–232; available at http://ieeexplore.ieee.org/document/1546627/.

[14]V. N. Popov, "Curvature effects on the structural, electronic and optical properties of isolated single-walled carbon nanotubes within a symmetry-adapted non-orthogonal tight-binding model," New J. Phys. **6**, 17 (2004).

[15]F. Sols, M. MacUcci, U. Ravaioli, and K. Hess, "Theory for a quantum modulated transistor," J. Appl. Phys. **66**, 3892–3906 (1989).

[16]M. Graf and P. Vogl, "Electromagnetic fields and dielectric response in empirical tight-binding theory," Phys. Rev. B **51**, 4940–4949 (1995).

[17]X. Pi and C. Delerue, "Tight-binding calculations of the optical response of optimally p-doped Si nanocrystals: A model for localized surface plasmon resonance," Phys. Rev. Lett. **111**, 177402 (2013).

[18]C. Jirauschek and T. Kubis, "Modeling techniques for quantum cascade lasers," Appl. Phys. Rev. **1**, 011307 (2014).

[19]J. Lee, S. Ganguli, A. K. Roy, and S. C. Badescu, "Density functional tight binding study of β-Ga_2O_3: Electronic structure, surface energy, and native point defects," J. Chem. Phys. **150**, 174706 (2019).

[20]I. Souza, N. Marzari, and D. Vanderbilt, "Maximally localized Wannier functions for entangled energy bands," Phys. Rev. B **65**, 035109 (2002).

[21]D. Gresch, Q. Wu, G. W. Winkler, R. Häuselmann, M. Troyer, and A. A. Soluyanov, "Automated construction of symmetrized Wannier-like tight-binding models from *ab initio* calculations," Phys. Rev. Mater. **2**, 103805 (2018).

[22]I. Souza, N. Marzari, D. Vanderbilt, M. Higashiwaki, K. Sasaki, A. Kuramata, T. Masui, S. Yamakoshi, J. Jung, A. H. Macdonald, H. Peelaers, C. G. Van de Walle, D. Gresch, Q. Wu, G. W. Winkler, R. Häuselmann, M. Troyer, A. A. Soluyanov, C. Franchini, R. Kováčik, M. Marsman, S. Sathyanarayana Murthy, J. He, C. Ederer, G. Kresse, S. Fang, R. Kuate Defo, S. N. Shirodkar, S. Lieu, G. A. Tritsaris, E. Kaxiras, S. Carr, S. Fang, H. C. Po, A. Vishwanath, and E. Kaxiras, "*Ab initio* tight-binding Hamiltonian for transition metal dichalcogenides," Phys. Rev. B **92**, 1–15 (2012).

[23]D. Papaconstantopoulos and M. Mehl, "The Slater–Koster tight-binding method: A computationally efficient and accurate approach," J. Phys.: Condens. Matter **15**, R413–R440 (2003).

[24]M. Nakhaee, S. A. Ketabi, and F. M. Peeters, "Tight-binding studio: A technical software package to find the parameters of tight-binding Hamiltonian," Comput. Phys. Commun. **254**, 107379 (2020).

[25]P. Giannozzi, S. Baroni, N. Bonini, M. Calandra, R. Car, C. Cavazzoni, D. Ceresoli, G. L. Chiarotti, M. Cococcioni, I. Dabo, A. Dal Corso, S. de Gironcoli, S. Fabris, G. Fratesi, R. Gebauer, U. Gerstmann, C. Gougoussis, A. Kokalj, M. Lazzeri, L. Martin-Samos, N. Marzari, F. Mauri, R. Mazzarello, S. Paolini, A. Pasquarello, L. Paulatto, C. Sbraccia, S. Scandolo, G. Sclauzero, A. P. Seitsonen, A. Smogunov, P. Umari, and R. M. Wentzcovitch, "QUANTUM ESPRESSO: A modular and open-source software project for quantum simulations of materials," J. Phys.: Condens. Matter **21**, 395502 (2009).
[26]J. P. Perdew, K. Burke, and M. Ernzerhof, "Generalized gradient approximation made simple," Phys. Rev. Lett. **77**, 3865–3868 (1996).
[27]J. P. Perdew, A. Ruzsinszky, G. I. Csonka, O. A. Vydrov, G. E. Scuseria, L. A. Constantin, X. Zhou, and K. Burke, "Restoring the density-gradient expansion for exchange in solids and surfaces," Phys. Rev. Lett. **100**, 136406 (2008).
[28]V. Zade, B. Mallesham, S. Shantha-Kumar, A. Bronson, and C. V. Ramana, "Interplay between solubility limit, structure, and optical properties of tungsten-doped Ga_2O_3 compounds synthesized by a two-step calcination process," Inorg. Chem. **58**, 3707–3716 (2019).
[29]M. Marezio and J. P. Remeika, "Bond lengths in the α-Ga_2O_3 structure and the high-pressure phase of $Ga_{2-x}Fe_xO_3$," J. Chem. Phys. **46**, 1862–1865 (1967).
[30]N. Ishizawa, T. Miyata, I. Minato, F. Marumo, and S. Iwai, "A structural investigation of α-Al_2O_3 at 2170 K," Acta Cryst. **36**, 228–230 (1980).
[31]H. Peelaers and C. G. Van de Walle, "Brillouin zone and band structure of β-Ga_2O_3," Phys. Status Solidi B **252**, 828–832 (2015).
[32]Y. Zhang, A. Neal, Z. Xia, C. Joishi, J. M. Johnson, Y. Zheng, S. Bajaj, M. Brenner, D. Dorsey, K. Chabak, G. Jessen, J. Hwang, S. Mou, J. P. Heremans, and S. Rajan, "Demonstration of high mobility and quantum transport in modulation-doped β-$(Al_xGa_{1-x})_2O_3/Ga_2O_3$ heterostructures," Appl. Phys. Lett. **112**, 173502 (2018).
[33]M. Mohamed, C. Janowitz, I. Unger, R. Manzke, Z. Galazka, R. Uecker, R. Fornari, J. R. Weber, J. B. Varley, and C. G. Van de Walle, "The electronic structure of β-Ga_2O_3," Appl. Phys. Lett. **97**, 211903 (2010).
[34]C. Janowitz, V. Scherer, M. Mohamed, A. Krapf, H. Dwelk, R. Manzke, Z. Galazka, R. Uecker, K. Irmscher, R. Fornari, M. Michling, D. Schmeißer, J. R. Weber, J. B. Varley, and C. G. Van de Walle, "Experimental electronic structure of In_2O_3 and Ga_2O_3," New J. Phys. **13**, 085014 (2011).
[35]K. Ghosh and U. Singisetti, "*Ab initio* velocity-field curves in monoclinic β-Ga_2O_3," J. Appl. Phys. **122**, 035702 (2017).
[36]K. Ghosh and U. Singisetti, "Impact ionization in β-Ga_2O_3," J. Appl. Phys. **124**, 085707 (2018).
[37]A. Singh, O. Koksal, N. Tanen, J. McCandless, D. Jena, H. G. Xing, H. Peelaers, and F. Rana, "Intra- and inter-conduction band optical absorption processes in β-Ga_2O_3," Appl. Phys. Lett. **117**, 072103 (2020).
[38]D. Shinohara and S. Fujita, "Heteroepitaxy of corundum-structured α-Ga_2O_3 thin films on α-Ga_2O_3 substrates by ultrasonic mist chemical vapor deposition," Jpn. J. Appl. Phys. **47**, 7311–7313 (2008).
[39]R. H. French, "Electronic band structure of Al_2O_3, with comparison to AlON and AlN," J. Am. Ceram. Soc. **73**, 477–489 (1990).
[40]G. Pizzi, V. Vitale, R. Arita, S. Blügel, F. Freimuth, G. Géranton, M. Gibertini, D. Gresch, C. Johnson, T. Koretsune, J. Ibañez-Azpiroz, H. Lee, J.-M. Lihm, D. Marchand, A. Marrazzo, Y. Mokrousov, J. I. Mustafa, Y. Nohara, Y. Nomura, L. Paulatto, S. Poncé, T. Ponweiser, J. Qiao, F. Thöle, S. S. Tsirkin, M. Wierzbowska, N. Marzari, D. Vanderbilt, I. Souza, A. A. Mostofi, and J. R. Yates, "Wannier90 as a community code: New features and applications," J. Phys.: Condens. Matter **32**, 165902 (2020).
[41]R. Wang, E. A. Lazar, H. Park, A. J. Millis, and C. A. Marianetti, "Selectively localized Wannier functions," Phys. Rev. B **90**, 165125 (2014).
[42]S. Coh and D. Vanderbilt, "Python tight binding (PythTB)" (2013).
[43]P. Vogl, H. P. Hjalmarson, and J. D. Dow, "A semi-empirical tight-binding theory of the electronic structure of semiconductors," J. Phys. Chem. Solids **44**, 365–378 (1983).
[44]S. Mu, H. Peelaers, Y. Zhang, M. Wang, and C. G. Van de Walle, "Orientation-dependent band offsets between $(Al_xGa_{1-x})_2O_3$ and Ga_2O_3," Appl. Phys. Lett. **117**, 252104 (2020).
[45]G. C. Kallinteris, N. I. Papanicolaou, G. A. Evangelakis, and D. A. Papaconstantopoulos, "Tight-binding interatomic potentials based on total-energy calculation: Application to noble metals using molecular-dynamics simulation," Phys. Rev. B **55**, 2150–2156 (1997).
[46]R. E. Cohen, M. J. Mehl, and D. A. Papaconstantopoulos, "Tight-binding total-energy method for transition and noble metals," Phys. Rev. B **50**, 14694 (1994).